Chapter 4

Bose-Einstein Condensation in a Circular Geometry

This chapter discusses quantum degenerate gases in a circular waveguide; the work in this chapter was presented in the publication:

- *S. Gupta, K. W. Murch, K. L. Moore, T. P. Purdy, and D. M. Stamper-Kurn, Bose-Einstein condensation in a circular waveguide, Phys. Rev. Lett. **95**, 143201 (2005). Included in Appendix G.*

As discussed in the preceding chapter, the primary difference between the millitrap and its larger counterparts are the comparatively large field curvatures arising from the millimeter length scales of the electromagnets. Beyond the described advantages for Ioffe-Pritchard traps, these field curvatures can be exploited in other trapping geometries as well. Specifically, we consider how to utilize the coaxial curvature and anti-bias coils to create a balanced, circular magnetic waveguide for ultracold atoms.

4.1   The Magnetic Quadrupole Ring

To explain the origin of the magnetic quadrupole ring (Q-ring), we look back to the Ioffe-Pritchard field in Equation (3.1) and envision eliminating the transverse gradient field $B'_\rho \to 0$. $\mathbf{B}_c$ now has a local field *saddle point* at the origin, and the field decreases for

$z = 0$, $\rho \gtrsim 0$ according to

$$\mathbf{B}_c = B_o\hat{z} + \frac{B_z''}{2}\left[\left(z^2 - \frac{\rho^2}{2}\right)\hat{z} - z\rho\hat{\rho}\right].\tag{4.1}$$

This field $\mathbf{B}_c$ vanishes in the $x - y$ plane at a radius of $\rho_o = 2\sqrt{B_o/B_z''}$. While the magnitude of the field expands linearly from this radius, the quadrupolar field differs from that of the spherical quadrupole considered in chapter 2. The magnitude of the gradient can be shown to be $B' = \sqrt{B_o B_z''}$, but it is the form of the field which distinguishes it from the spherical quadrupole. More precisely, about a point at $(z = 0, \rho = \rho_o)$, it is the case that

$$\frac{\partial \mathbf{B}_c}{\partial z} \cdot \hat{z} = 0 \quad , \quad \frac{\partial \mathbf{B}_c}{\partial \rho} \cdot \hat{\rho} = 0$$
$$\frac{\partial \mathbf{B}_c}{\partial \rho} \cdot \hat{z} = -B' \quad , \quad \frac{\partial \mathbf{B}_c}{\partial z} \cdot \hat{\rho} = -B',\tag{4.2}$$

and $\partial \mathbf{B}_c/\partial\theta = 0$ trivially from cylindrical symmetry. This should be contrasted with the spherical quadrupole field, which has a field profile of $\mathbf{B}_{SQ} = B_{SQ}'(x, y, -2z)$. Graphically, the Q-ring and its field lines are depicted in Figure 4.1.
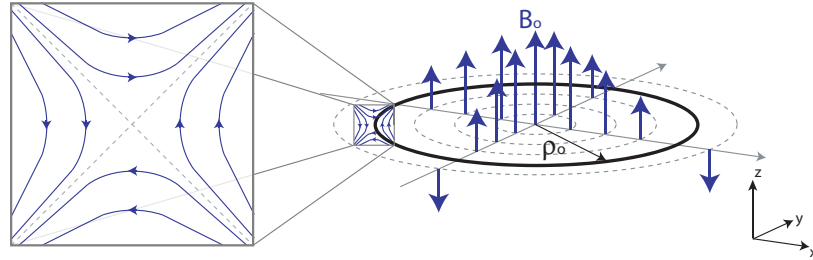

Figure 4.1: Quadrupolar Ring Diagram.

Assuming the z-axis is aligned with the direction of the gravitational acceleration g, the locus of field zeros will be a local magnetic field minimum if $B' > |mg/\mu|$. Thus, in its ideal form, the Q-ring is a perfectly flat and circular magnetic quadrupole trap.

4.2   Corrections to the Cylindrically Symmetric Q-ring

Of course, ideal cylindrical symmetry is difficult to achieve. In this section, we explore scenarios where this symmetry is broken in both controlled and uncontrolled manners. The

consequences of a departure from a perfectly flat ring are significant for ultracold atoms because of the minuscule energy scales involved. Thus, we consider field modifications from various perturbative corrections, as well as the energetic modification for a particle, of magnetic moment μ, confined in the waveguide.

4.2.1   Bias Fields

Suppose a uniform bias field $\mathbf{B}_s = B_s \hat{s}$ is applied to the Q-ring field in Equation (4.1), where $\hat{s}$ is an arbitrary unit vector. We immediately see that z-component of $\mathbf{B}_s$ is merely absorbed into an offset of the bias field of $\mathbf{B}_c$, i.e. $B_o \rightarrow B_o + \mathbf{B}_s \cdot \hat{z}$. This changes the radius ρ_o but maintains the cylindrical symmetry which gives the circular locus of field zeros.

Therefore, we need only consider bias fields in the x-y plane of the ring, with two relevant parameters being the magnitude B_s and the angle θ_s off the heretofore arbitrary x-axis. The field of the Q-ring thus becomes:

$$\mathbf{B}_c = B_o \hat{z} + \frac{B_z''}{2}\left(z^2 - \frac{\rho^2}{2}\right)\hat{z} + \left[B_s \cos(\theta - \theta_s) - z\rho\right]\hat{\rho} - B_s \sin(\theta - \theta_s)\hat{\theta}. \qquad (4.3)$$

Some further algebra reveals that the field near the unperturbed ring behaves as

$$\mathbf{B}_c = -B'\rho\hat{z} + \left[B_s \cos(\theta - \theta_s) - B'z\right]\hat{\rho} - B_s \sin(\theta - \theta_s)\hat{\theta}. \qquad (4.4)$$

Unlike the perfect ring field of Equation (4.1), this field vanishes at only two points $-$ $(B_s/B', 0, \theta_s)$ and $(-B_s/B', 0, \theta_s + \pi)$ $-$ in (z, ρ, θ) coordinates. This tilts and stretches the ring in the $z - \theta_s$ plane by an angle $\phi_{tilt} = \tan^{-1}\left(\frac{B_s}{2B_o}\right)$. This deformation does *not* correspond to a pure rotation, such as would result from just tilting the entire trapping assembly. The circular field has been deformed to maintain the ρ_o circular projection on the $x - y$ plane (depicted in Figure 4.2).

The modification to the potential around the ring is two-fold. First, a particle will experience a magnetic contribution to the energy as $\mu B_s |\sin(\theta - \theta_s)|$. Second, the tipping of the ring will cause a gravitational contribution to the energy shift if the field minimum at θ is lifted/lowered off $z = 0$. Together, the potential felt by a magnetic particle in the ring would, to lowest order, be given by

$$U(z, \theta) = mgz + \mu\sqrt{\left[B_s \cos(\theta - \theta_s) - B'z\right]^2 + B_s^2 \sin^2(\theta - \theta_s)}. \qquad (4.5)$$
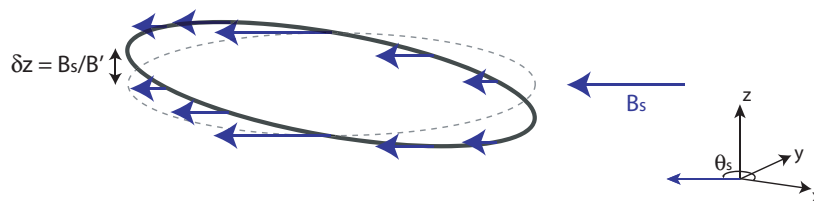
Figure 4.2: Q-ring under transverse bias field.

As previously stated, it must be the case that $B_z'' \gg |mg/\mu|$ to effect magnetic trapping against gravity. This condition guarantees that the potential energy gained by the vertical displacement at θ_s, $\Delta U_{grav} = mg(B_s/B')$, is less than the magnetic potential energy at $\theta_s \pm \pi/2$, $\Delta U_{mag} = \mu B_s$. This is best seen in a contour plot of Equation (4.5) on z and θ, shown in Figure 4.3:
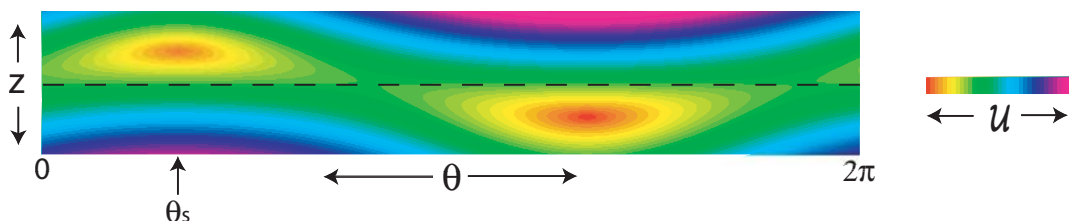

Figure 4.3: Gravi-magnetic potential contour plot.

As expected, $\theta_s + \pi$ is the energetic minimum of the ring, vertically displaced below the ring. A second local energy minimum occurs at θ_s, but displaced *above* the unperturbed $z = 0$ ring by B_s/B'. Finally, we are interested in the energetic variation of the potential around the ring, $\mathcal{U}(\theta)$, which is defined to be the minimal value of the potential at a given cylindrical angle θ. This is most readily obtained by setting the derivative of (4.5) with respect to z to zero and solving, but some care must be taken. The magnetic potential energy must be everywhere positive for a magnetically-trappable particle which remains adiabatic in the ring. With this consideration, $U(\theta)$ can be shown to have the form

$$U(\theta) = \mu B_s \left[\left(\sqrt{1 + f_2^2} + f_2 \right) |\sin(\theta - \theta_s)| + f_1 \cos(\theta - \theta_s) \right], \qquad (4.6)$$

where $f_1 \equiv mg/\mu B'$ and $f_2 \equiv mg/\sqrt{(\mu B')^2 + (mg)^2}$. The presence of the *absolute value* of $\sin(\theta - \theta_s)$ is of course representative of the fact that the magnetic potential energy is manifestly positive about the ring. That this potential contains high-order harmonics (all even, as a matter of fact) has important implications for the motion of propagating atoms, a detailed consideration of which may be found in our paper on betatron resonances [53].

4.2.2   Gravity

Even in the absence of external bias fields, gravity can play a role if the symmetry axis of the electromagnetic coils is not aligned with the gravitational acceleration, **g**. If the coil axis is kept as the z-axis, then the **g** can be given as $\mathbf{g} = -g(\cos\phi, \sin\phi\cos\theta_g, \sin\phi\sin\theta_g)$, where ϕ is the angle between **g** and $\hat{z}$, and θ_g is angle formed between the $x - y$ projection of **g** and the $x - y$ plane. The potential variation around the ring can then be written as

$$U(z, \rho, \theta) = \mu B'\sqrt{z^2 + (\rho - \rho_o)^2} + mgz\cos\phi + mg\rho\sin\phi\cos(\theta - \theta_g), \qquad (4.7)$$

At a given θ, this equation is trivially minimized with $z = 0$, $\rho = \rho_o$. The energetic variations about the waveguide path, however, can vary substantially

$$U(\theta) = mg\rho_o\sin\phi\cos(\theta - \theta_g), \qquad (4.8)$$

with $\phi \to \pi/2$ and a sizeable ρ_o being the most obvious scenario. Unlike Equation (4.6), Equation (4.8) has only a first-order harmonic term in θ. This fact disallows any rebalancing of a gravitationally misaligned Q-ring using only an external bias field. Rather, a combination of bias and curvature fields is needed.

4.2.3   Inhomogeneous Fields

Moving beyond simple bias fields, an arbitrary inhomogeneous vector field $\mathbf{B}_{ext}(x, y, z)$ may be applied to the ring. As a simple bias field already added a non-trivial $|\sin\theta|$ modification to the potential energy variations about the ring, we can expect sizable inhomogeneous external fields to further complicate the energetic structure of the ring. A severe case of this is depicted in Figure 4.4:
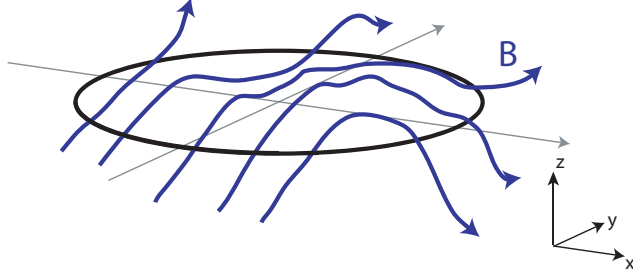
Figure 4.4: The Q-ring in the presence of inhomogeneous magnetic fields.

We may consider these fields generally in a fourier expansion about the locus of the unperturbed ring as

$$\mathbf{B}(\theta) = \sum_{l=0}^{\infty} \mathbf{B}_l \sin(l\theta - \theta_l) \,. \tag{4.9}$$

This is not immediately useful, as the fields may expand, stretch, and displace the shape of the ring. Further, the field moments $\mathbf{B}_l$ and phases ϕ_l are unknown, as is their relationship to the relevant magnetic ring quantities, B_o, B', B_z''. This does suggest, however, that we might similarly examine the deformation of the ring and the potential function about the ring minima in harmonic terms:

$$\mathbf{r}_{ring} \to \sum_{l=0}^{\infty} \left(\delta z_l \sin(l\theta - \phi_{z,l})\hat{z} + \delta \rho_l \sin(l\theta - \phi_{\rho,l})\hat{\rho} \right) \tag{4.10a}$$

$$U(\theta) \to \sum_{l=0}^{\infty} \frac{U_l}{2} \left(1 + \sin(l\theta - \phi_l) \right) , \tag{4.10b}$$

where the energetic moments are measured off the $U = 0$ flat ring. The magnitude of the δz_l, $\delta \rho_l$, and U_l moments can be related back to the various orders of spatial derivatives of $\mathbf{B}_{ext}(x, y, z)$, but ultimately the central meaning of Equation (4.10) lies in the relation of the higher-order harmonic structure of the ring to the field inhomogeneities. As noted in Subsection 4.2.1, these harmonics are important for the motion of atomic beams about the ring, with the connection explored extensively in Ref. [53].

4.3   Loading Atoms into the Q-Ring

The first observation of the Q-ring came as a bit of a surprise, although it was ac-
complished in precisely the manner discussed in Section 4.1. Atoms were trapped in the
Ioffe-Pritchard configuration and the gradient current controlling B'_ρ was progressively re-
duced to zero. As this was carried out, the atoms were pulled from the IP trap center and
began filling in the Q-ring.

This is hardly the ideal manner to load atoms into the Q-ring, and while the atoms
were delivered in a manner identical to that discussed in the previous chapter, the best
"handshaking" between the external quadrupole trap and the Q-ring was to heavily bias the
Q-ring along $-\hat{y}$, the entry axis for the atoms coming from the loading region. The atoms
are transferred to the tilted Q-ring just as they were to the millitrap spherical quadrupole
trap, a procedure which is depicted in Figure 4.5. More quantitatively, 2.5×10^7 atoms,
pre-cooled to $60\,\mu\text{K}$ were confined in the $200\,\text{G/cm}$ field from the external quadrupole
transfer coils. Within $1\,\text{second}$, the spherical quadrupole field was converted to a tilted
Q-ring trap produced with $B''_z = 5300\,\text{G/cm}^2$, $B_o = 22\,\text{G}$, and a side field of magnitude
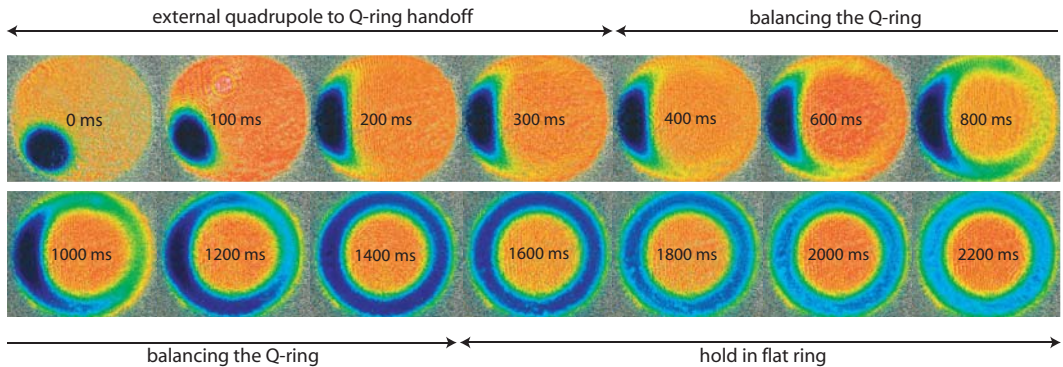$B_s = 9.2\,\text{G}$. This process left 2×10^7 atoms trapped in the tilted Q-ring.

Figure 4.5: Time sequence of loading atoms into the Q-ring. In the first $500\,\text{ms}$, the atoms
bound in the external quadrupole coils are aligned with the left edge of the Q-ring. The
millitrap current is engaged (in a $9\,\text{G}$ tilted Q-ring setting) as the external quadrupole trap
is ramped off. Reorienting the Q-ring is then accomplished by bias field shifts, and in the
case shown the ring is slowly balanced over the course of $1\,\text{second}$. In the balanced ring,
the Majorana loss rate is increased (see text) and the population fades at an accelerated
pace.

The bias field which tips the ring may itself be extinguished to balance the Q-ring, a sequence also shown in Figure 4.5. As the atoms fill the flattened Q-ring, a noticeable increase in the loss rate is observed. The origin of this increase, of course, comes from the fact that the Q-ring is an unbiased magnetic trap, susceptible to the same Majorana spin-flip losses which plague spherical quadrupole traps. We note here that the normal experimental operation only made use of the first $500\,\mathrm{ms}$ of Figure 4.5, i.e. the *Q-ring* was never actually flattened in practice. A method to bias the Q-ring and maintain the circular structure is discussed later, and this technique was employed directly in the tilted Q-ring which suffers less from Majorana losses for reasons which we will now explore.

4.4   Majorana Losses in the Q-Ring

Majorana losses are a well-known phenomenon in ultracold atomic physics precluding the use of DC current spherical quadrupole traps to achieve BEC [21]. The central idea is contained in a recognition of the fact that a magnetically-trapped spin state $|F = 1, m_F = -1\rangle$ is Larmor precessing in its *local* magnetic field at a rate $\omega_L = \frac{1}{2}\mu_B|\mathbf{B}(x, y, z)|$. Near the center of a spherical quadrupole trap the field vanishes, which means that the Larmor precession frequency of atoms near the origin can be quite small. To remain adiabatic and in a trappable state, the time rate of change of atomic orientiation must be substantially less than ω_L. In the case at hand of a spin in a magnetic field, this can be expressed as

$$\frac{\partial}{\partial t}\frac{|\hat{\mu} \cdot \mathbf{B}|}{|\mu|\,|\mathbf{B}|} \ll \frac{\mu|\mathbf{B}|}{\hbar}\,. \tag{4.11}$$

If this condition is violated then the system is open to "spin flips," in that the particles will have non-zero amplitude to be in other spin states which are untrapped. To estimate the amount of loss that a system of thermal atoms would experience in a spherical quadrupole trap of gradient B', we look to the critical radius r_c at which the two expressions in Equation 4.11 are equal:

$$\frac{v}{r_c} = \frac{\mu_B B' r_c}{\hbar}\,, \tag{4.12}$$

where v is the velocity of the atom. Within factors of unity, we can say that for a thermal gas of average velocity $v \approx \sqrt{k_B T/m}$ the critical radius is

$$r_c \approx \sqrt{\frac{\hbar}{\mu B'} \sqrt{\frac{2 k_B T}{m}}} \, . \tag{4.13}$$

We also note that the thermal cloud occupies a volume of $V \approx \pi (k_B T/\mu_B B')^3$. Together these elements translate to a Majorana loss rate Γ_M by considering the thermal flux of atoms through the surface boundary of $A_c = 4\pi r_c^2$, which can be shown to be

$$
\begin{aligned}
\Gamma_M &\approx \frac{A_c}{V} \sqrt{\frac{2 k_B T}{m}} \\
&\approx 6 \frac{\hbar}{m} \left(\frac{\mu_B B'}{k_B T} \right)^2 \, .
\end{aligned}
\tag{4.14}
$$

If we extend this analysis to the Q-ring, we recognize that the critical radius r_c does not change, but instead of enclosing an ellipsoid it bounds a torus of radius ρ_o. Thus, the surface boundary is given by $A_c = 2\pi \rho_o r_c$, the volume becomes $V = 2\pi^2 \rho_o (k_B T/2\mu B')^2$, and the Majorana loss rate is

$$\Gamma_M \approx \frac{\hbar^{1/2}}{\pi m^{3/4}} \frac{(\mu B')^{3/2}}{(k_B T)^{5/4}} \, . \tag{4.15}$$

The absence of any ρ dependence is initially surprising, but is merely a reflection of the fact that in a torus the surface area to volume ratio is constant with radius.

Regarding specifically our Q-ring, we attempted to quantify these losses at various Q-ring tilts. For a ring of $B_o = 22\,\mathrm{G}$, $B_z'' = 5300\,\mathrm{G/cm^2}$, a variable bias field B_s along the y-axis was applied and the atom loss rate for a $T = 60\,\mu\mathrm{K}$ cloud measured, shown in Figure 4.6.

For these experimental values, the expression in Equation (4.15) would predict a loss rate of $6\,/\mathrm{s}$, far in excess of the maximal $0.3\,/\mathrm{s}$. This is almost certainly due to residual fields, perhaps even sizeable inhomogeneous fields, which mitigate some of the Majorana damage that the flat ring prediction of Equation (4.15) would predict. This foreshadows a result presented later in this chapter for the energetic variations in the ring, but whatever the cause the Q-ring, like its spherical quadrupole counterpart, is incapable of accommodating a quantum degenerate sample. We now turn to a method which will eliminate these losses in the ring, facilitating Bose condensation in the ring.
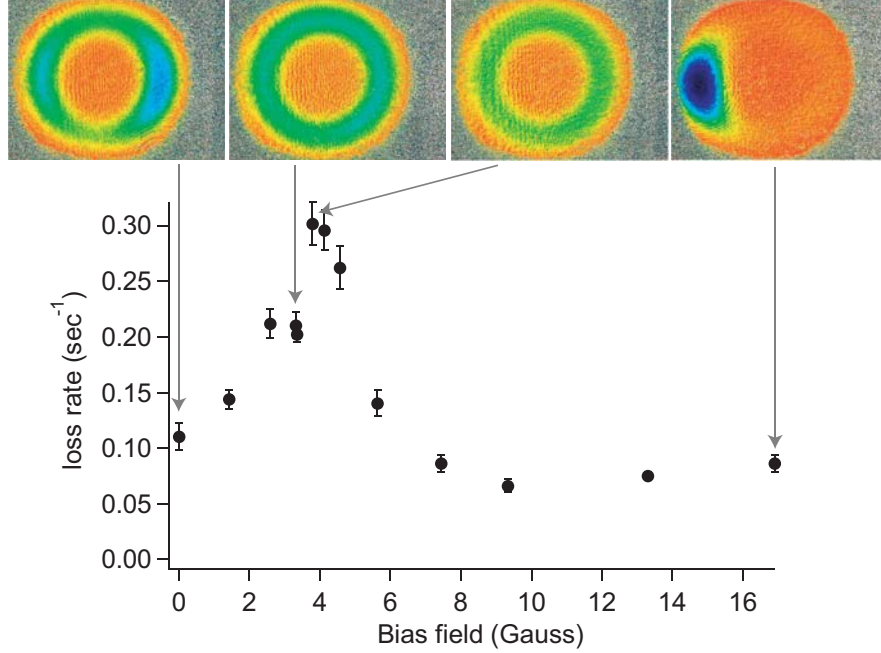
Figure 4.6: Variation of Majorana loss rate with Q-ring tip. The Majorana loss rate is measured as function of bias field, showing the increased loss rate in the balanced configuration versus tipped configuration. Absorption images are associated with the observed loss rates in the data series. With this method, we were able to diagnose not only the Q-ring but the permanent magnetic field inside our vacuum chamber to be $\approx -3.7\,\mathrm{G}\hat{y}$.

4.5   The Time-Orbiting Ring Trap

Just as the Majorana losses from a spherical quadrupole trap can be eliminated by the orbiting field of the TOP trap, we look to orbiting fields to reduce the deleterious effect of the field zero. To make the Q-ring equivalent of a TOP trap, we employ a Time-Orbiting Ring Trap (TORT) [85] which consists of the following field

$$\mathbf{B}_r = B_r\big(\cos(\omega_r t), \sin(\omega_r t), 0\big), \tag{4.16}$$

and is most readily accomplished by the application of an oscillating axial bias field $\mathbf{B}_{r,1} = B_r(\cos \omega_r t, 0, 0)$ and spherical quadrupole field $\mathbf{B}_{r,2} = \frac{B_r}{\rho_o}\sin \omega_r t\,(-z, \rho, 0)$, all expressed in (z, ρ, θ) coordinates. This field must be added to the arbitrarily biased Q-ring field in

Equation (4.3). In this case, the field about the unperturbed ring is

$$\mathbf{B}_c = \left(B_r \cos \omega_r t - B' \rho \right) \hat{z} + \left(B_r \sin \omega_r t + B_s \cos(\theta - \theta_s) - B' z \right) \hat{\rho} - B_s \sin(\theta - \theta_s) \hat{\theta} . \quad (4.17)$$

As in Section 3.5.3, we take the time-averaged field to second-order in $|B'r/B_r|$ about the minimal azimuthal path and obtain the field magnitude

$$|\mathbf{B}_c| = B_{eff} + \frac{B'^2}{2B_{eff}} \left(1 - \frac{1}{2} \frac{B_r^2}{B_{eff}^2} \right) \left(\rho^2 + z^2 \right) , \quad (4.18)$$

where $B_{eff} = \sqrt{B_r^2 + B_s^2 \sin^2(\theta - \theta_s)}$. It is worth noting that the base transverse trapping frequency from this field profile, $\omega_T = \sqrt{\frac{\mu}{m} \frac{B'^2}{2B_r}}$, is everywhere reduced by the application of B_s except at $\theta - \theta_s = 0, \pi$ where it is unchanged.

If we consider a ring which is also tipped slightly ($\phi \ll 1$) at angle θ_g with respect to gravity, then to lowest order the potential about the ring can be shown to be

$$U(\theta) = \mu \sqrt{B_r^2 + B_s^2 \sin(\theta - \theta_s)} + mgh \cos(\theta - \theta_g) + mg \frac{B_s}{B'} \cos(\theta - \theta_s) , \quad (4.19)$$

where $h = \rho_o \sin \phi$, the height of the tilt in the ring. It is worth noting here that the rotating field B_r can, in the appropriate limit, "smooth out" the absolute value asymmetry of the $B_s |\sin(\theta - \theta_s)|$ which doomed the balancing of the Q-ring in Equation (4.6). For $B_r \gg B_s$, the TORT may be completely flattened against slight gravitational misalignments with only energetic variations of $\mu \left(\frac{B_s}{2B_r} \right) B_s |\sin(\theta - \theta_s)|$, a significant improvement over the $B_s |\sin(\theta - \theta_s)|$ of the Q-ring.

4.6   Topping Off the Q-ring

The time-varying fields needed to convert our Q ring to the TORT traps were obtained by suitably modulating the currents in the four coils used to generate the Q-ring potential. A rotating field frequency of 5 kHz was found to yield the best conditions, easily satisfying the requirement to be much larger than the transverse motional frequencies (< 100 Hz) and also much smaller than the Larmor precession frequency (> 3 MHz). To first switch on the TORT, a rotating field magnitude of $B_{rot} = 18$ G was used.

As shown in Figure 4.7, the trap lifetime was dramatically increased by application of the TORT trap. In the first few seconds after switching on the TORT, we observed a
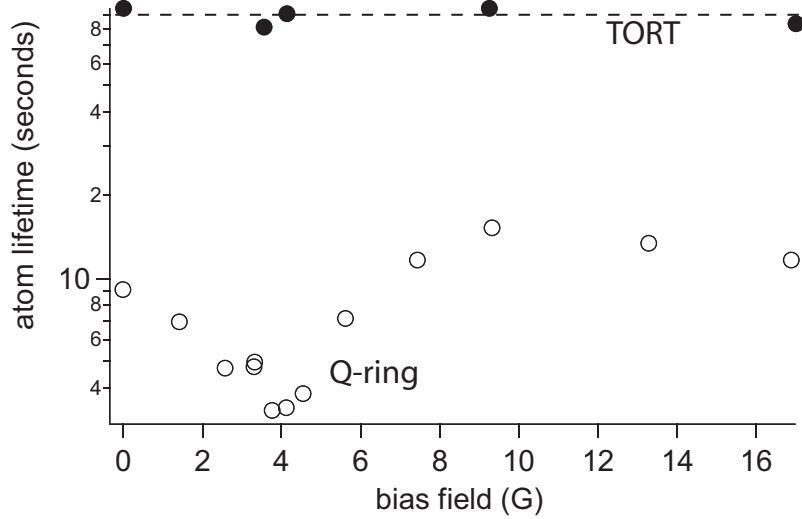
Figure 4.7: Elimination of Majorana losses in the TORT. The Q-ring loss rate data from Figure 4.6 (closed circles) are compared to the long lifetime in the TORT (solid circles). The TORT exhibits a vacuum limited lifetime of 90 seconds, irrespective of the orientation of the ring.

fast loss of atoms and a simultaneous drop in their temperature. We ascribe this loss and cooling to the evaporation of atoms from the trapped cloud to the finite depth of the trap. (This was affectionately referred to as the "torus of death.") As the temperature dropped, the evaporation rate diminished and the lifetime of trapped atoms became vacuum limited at 90 s, a value observed both for balanced and for tilted TORT traps.

4.7   BEC in the TORT

The long lifetime in the biased TORT makes possible the evaporation of the atoms to quantum degeneracy. Applying a $B_s \sim 9\,\text{G}$ bias field the TORT is "tipped" and the potential is given by that in Equation (4.19). To proceed to the BEC phase transition, we begin by utilizing the finite depth of the TORT as torus of death evaporation was applied by ramping down the rotating field strength B_{rot} over 40 s to 4.8 G. The oscillation frequencies in this trap were measured as $2\pi \times (87, 74.5, 35)\text{Hz}$, with the transverse asymmetry a consequence of the applied bias field. In the second stage, RF evaporation was applied for

20 s, yielding clouds of up to 6×10^5 atoms at the Bose-Einstein condensation temperature, and pure BECs of up to 3×10^5 atoms.

A natural goal would be the Bose condensation in not just the tipped TORT but the fully balanced TORT. To get an idea of the prospects of accomplishing this in our current configuration, we can estimate the transition temperature with the current experimental values of $N \sim 3 \times 10^5$ atoms, $\omega_T = 2\pi \times 85\,\mathrm{Hz}$, and $\rho_o = 1.25\,\mathrm{mm}$. BEC occurs for the phase space density $\Gamma = N\lambda_{dB}^3/V \sim 1$, so with the thermal volume of the ring given by

$$\begin{aligned} V &= (2\pi\rho_o) \times \left(\pi\sigma_T^2\right) \\ &= 2\pi^2\rho_o \left(\frac{k_B T}{m\omega_T^2}\right). \end{aligned} \tag{4.20}$$

With the thermal deBroglie wavelength $\lambda_{dB} = \sqrt{2\pi\hbar^2/mk_B T}$, we obtain the critical temperature (within factors of unity)

$$T_c = \frac{1}{k_B}\left[N^2 \left(\frac{\hbar^2}{m\rho^2}\right)(\hbar\omega_T)^2\right]^{1/5} \approx 40nK. \tag{4.21}$$

This is a very small temperature indeed, but hardly out of the realm of possibility when the transition temperatures for most BEC experiments are in the 100's of nK. A crucial distinction must be made, however, between comparing this temperature and that of harmonic traps. In previous sections of this chapter, we have discussed the energetic variations around the ring. The formula in Equation (4.21) relies on a perfectly flat ring, and this is unlikely to be the case. Surely we can tolerate potential variations no more than the transition temperature of the flat ring, which translate to a ring balanced to $500\,\mu\mathrm{G}$ around the circumference. This is a *very* flat ring and, as we will see, it is much flatter than our current implementation is capable of producing.

4.8   Motion in the Circular Waveguide

With the prospect of condensing the atoms in the current incarnation of the TORT looking grim, we "settled" on launching the atoms into motion about the circular waveguide. Our successful implementation of this led to the oft-used phrase *The Ultracold Atom Storage Ring*, somewhat in homage to the experts in experimental particle physics who have been studying the motion of particles in circular waveguides for over 65 years [86].

Using the motion of the atoms to probe the energetic structure of the ring led to even more connections to accelerator physics than we initially suspected, and is a prerequisite for any interferometry scheme to be implemented in the ring. In this Section, the basic elements of motion in the circular waveguide are explored, while the more detailed information about the atom beam motion is discussed in the subsequent chapter and Refs. [53, 55].

4.8.1   Azimuthal Oscillatory Motion

After condensing the atoms in the $B_s = 9\,\mathrm{G}$ biased TORT, the bias field may be shifted in magnitude and/or orientation. If the bias field is shifted slowly with respect to the atomic motion set by the trapping frequencies, then the cloud remains adiabatic and follows the ground state of the shifting trap minimum. If the bias field is reoriented rapidly, then the atoms will experience a net azimuthal force given by $-\frac{1}{\rho}\frac{\partial U}{\partial \theta}$ and be accelerated by the potential gradient. Assuming that the force is uniform across the spatial extent of the ensemble[1], the stationary atom cloud becomes a propagating atom beam which undergoes motion about the ring according to the potential $U(\theta, t)$.

In a simple case, we can consider rapidly, i.e. on a timescale faster than the $2\pi/\omega_\theta = 29\,\mathrm{ms}$, changing B_s from $9\,\mathrm{G}$ in the $-\hat{y}$-direction to $B_s = 9\,\mathrm{G}$ in the $\hat{x}$-direction. The atom cloud thus looks like a displaced oscillator in the modified $U(\theta)$, and the atoms will oscillate about the new minimum as shown in Figure 4.8(a).

In the presence of stray fields and gravitational misalignment, it is much easier to create an unbalanced biased ring than a flat, balanced ring. Oscillatory motion about a potential minimum in the ring is thus the norm and, insofar as motional oscillations of this sort are not terribly useful, much trial and error was required to *avoid* this scenario and set the atoms into unterminated propagation. Using the "shifted minimum" which accelerates the atoms was quite useful however, and made possible the following subsection which explores the range of motion where the atom beam propagates freely about the ring.

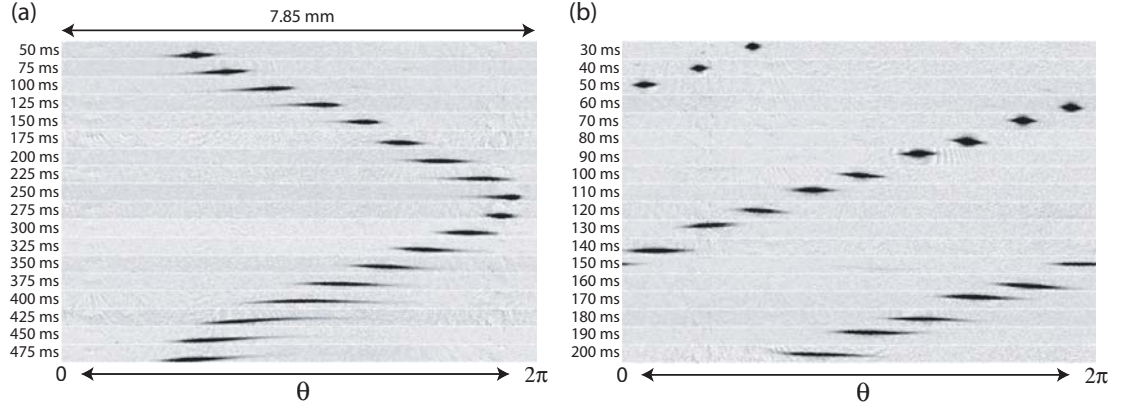[1]The validity of this assumption will be discussed in chapter 5.

Figure 4.8: Atomic beam motion in the waveguide. (a) Shown is the time sequence of an unsuccessful launch sequence. Absorption images are collected after $2\,\mathrm{ms}$ time-of-flight release from the waveguide potential, and then post-processed to show an annular strip from $1.10\,\mathrm{mm} < \rho < 1.35\,\mathrm{mm}$. The atoms are not accelerated enough to overcome the residual variations in $U(\theta)$. (b) A better acceleration and balancing of the TORT allows a successful launch of the atoms into unterminated motion about the ring. The trap settings for the launch herein were $B_{rot} = 12.6\,\mathrm{G}$ ($\omega_T \simeq 2\pi \times 50\,\mathrm{Hz}$), $B_o = 20\,\mathrm{G}$, $B_z''|_{z=0} = 5300\,\mathrm{G/cm^2}$, $\rho_o = 1.25\,\mathrm{mm}$, with a final angular (linear) velocity of $2\pi \times 6.4\,\mathrm{rad/s}$ ($50.6\,\mathrm{mm/s}$).

4.8.2   Unterminated Motion in the Waveguide

Guided by the amplitude and velocity of the oscillatory motion described in the preceding subsection, we discovered a "launching" regime whereby unterminated motion about the waveguide was possible. Optimal settings were accomplished by reorienting the sideways bias field B_s, inducing the trapped atoms to accelerate toward the newly positioned tilted TORT trap minimum (advanced by an azimuthal angle of about $\theta = \pi/4$) while simultaneously reducing the magnitude of B_s to $B_s \sim 0$. Much trial and error was required, but a narrow window of final transverse bias fields B_s allowed a ring balanced enough such that the kinetic energy imparted during the acceleration stage overcame the residual potential variations in the flattened ring.

The final value of B_{rot} was a free parameter from $4.8 - 13\,\mathrm{G}$, allowing a range of possible transverse trapping frequencies $\omega_T \simeq 2\pi \times (50 - 90)\,\mathrm{Hz}$ and maximum potential height of $k_B \times (40 - 100)\,\mu\mathrm{K}$ for the waveguide. Under successful launches, the atoms were allowed to propagate freely around the guide for various guiding times before being

observed by absorption imaging. Final angular velocities were possible over a range of $\Omega \simeq 2\pi \times (6-19)\,\text{Hz}$. A time sequence of an $\Omega = 11\,\text{Hz}$ launch is shown in Figure 4.8(b).

4.8.3   Diagnosing the Azimuthal Potential Variations

The next chapter discusses in detail the atomic beam in this free propagation state, but for the purposes here we can consider the unterminated motion categorically good from the perspective of making the Ultracold Atom Storage ring useful for applications such as Sagnac interferometry. While obtaining a relatively flat ring was a requirement to inject atoms into unterminated motion, the motion of the atoms about the ring can be used to balance the azimuthal potential even further. We can infer $U(\theta)$ by measuring the azimuthal variations in the kinetic energy of a beam propagating in the static ring potential. For this, we measured the center-of-mass position of the cloud vs. propagation time, and determined the velocity and energy from differences in this position vs. time. Figure 4.9 shows, for slight variations in a bias field along the y-axis, the measured kinetic energy as a function of azimuthal position.

Assuming the kinetic energy variations are due primarily to longitudinal potential energy variations, Figure 4.9(b) shows the "flattest" waveguide potential we were able to make. The data may be fit to the presumed azimuthal potential in Equation (4.19), shown as the solid curve in Figure 4.9(b). Further efforts were unsuccessful at reducing the potential energy variations below that shown, and thereby $5\,\mu\text{K}$ was taken as the "flattest" achievable ring. This is much higher than the tilted TORT BEC transition temperature of $\sim 100\,\text{nK}$, and higher still than the full-ring transition temperature of $T_c \sim 40\,\text{nK}$. With two orders of magnitude in ring flatness to bridge, we abandoned hope of condensing atoms into the full ring, leaving this task to the very capable next generation of experimentalists[2].

4.8.4   Expansion of the Atomic Beam

When the beam is released from the azimuthal confinement, the atoms will expand longitudinally as the mean field energy is rapidly converted into kinetic energy. This behavior is discussed in more detail in the following chapter, but briefly we may consider

---

[2]Tony Öttl, Ryan Olf, and Ed Marti are already hard at work.
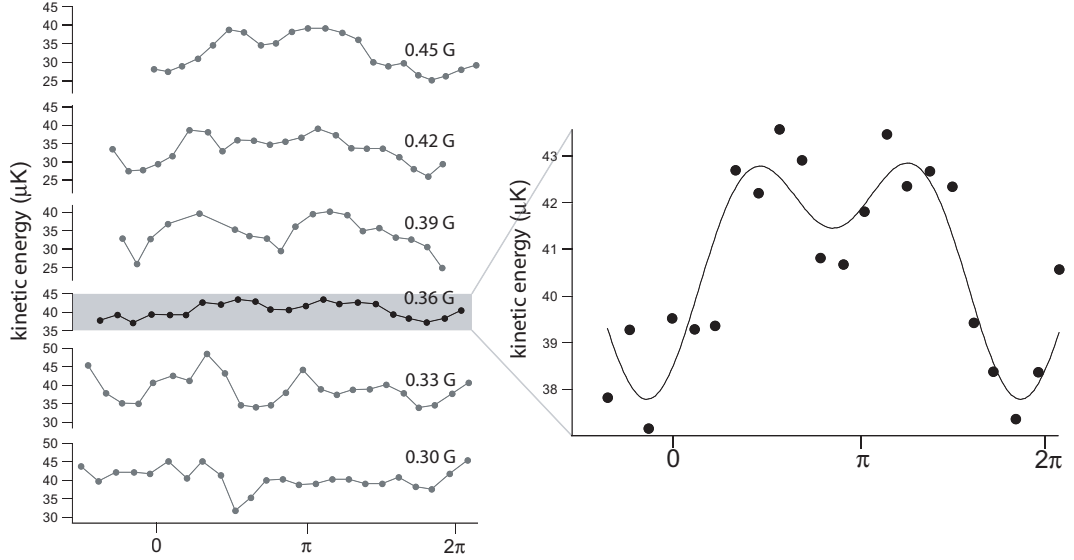
Figure 4.9: Azimuthal energy map of the circular waveguide as measured by atomic beam motion. (a) The tilt of the waveguide is controlled by a bias field along the y-axis, and the optimal setting of $B_y = 0.36\,\text{G}$ is seen in the small variations of the kinetic energy of the beam as it orbits the ring. (b) A magnification of the $B_y = 0.36\,\text{G}$ potential map shows that the kinetic energy, and thereby $U(\theta)$, exhibits at least $5\,\mu\text{K}$ of variation around the ring.

that the energy per particle in the Thomas-Fermi approximation is $E/N = \frac{5}{7}\mu$ [20]. This will be converted to a velocity spread across the cloud of $\sigma_v = \sqrt{\frac{10\mu}{7m}}$. In the trap described herein, the chemical potential for 3×10^5 atoms is $\mu = \hbar \times 2\pi \times 860\,\text{Hz}$, yielding a predicted rms longitudinal velocity spread of $1.7\,\text{mm/s}$.

This is expansion can be observed and quantified as the atom beam propagates around the ring, essentially providing unlimited time-of-flight until the atom beam begins to wrap around itself. Figure 4.10 shows the expanding beam after successive orbits around the ring, and the observed expansion rate of $1.8\,\text{mm/s}$ is in good agreement with the expected value.
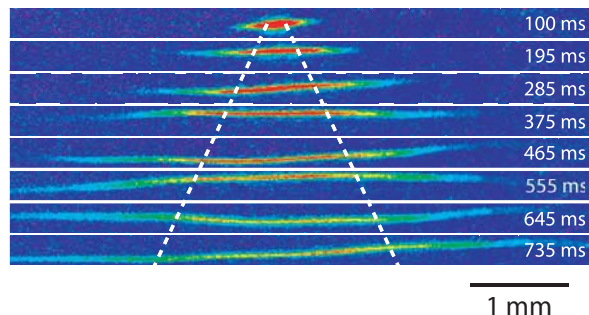
Figure 4.10: Mean-field driven expansion into the waveguide. As discussed in text, the mean-field energy released upon cessation of the longitudinal trap results in a 1.8 mm/s rms velocity width of the beam. Images shown were captured after successive laps around the ring at angular velocity $\Omega = 2\pi \times 11$ Hz. Dotted lines follow the uniformly expanding rms width.

4.9   Prospects for Sagnac Interferometry

One of the most exciting potential applications of the circular atom waveguide would be its use as a sensitive rotation sensor. The use of atom interferometry for a gyroscopic measurement has already proven a short-term sensitivity better than the best ring laser gyroscopes [87]. The principle of operation is based on the Sagnac effect [88], where an interferometric signal based on splitting a wave into counter-propagating beams which traverse a beam path that encloses an area A. The beams recombine and the relative phase is measured. If this measurement is conducted in a rotating frame Ω, then the effective path length is increased (decreased) for the beam traveling in the same (opposite) direction as the rotation. The relative phase between the waves at recombination is

$$\delta\phi = \frac{8\pi\Omega A}{\lambda v} \,. \tag{4.22}$$

This was derived for light, but is valid for matter waves of $\lambda = h/p$, which gives the matter Sagnac phase shift to be

$$\delta\phi = \frac{4m\Omega A}{\hbar} \,. \tag{4.23}$$

The sensitive atom gyroscope of Kasevich et al. [87] was implemented in free space. As ultracold atom techniques have become more refined, the use of atom waveguides to engineer an area-enclosing beam path has garnered much interest and experimental investigation

in recent years [89, 90, 91].

Achieving Sagnac interferometry in the circular waveguide described in this chapter is an attractive experimental avenue, especially due to the possibility of employing optical atom beamsplitters (discussed in the next section) which are useful in this context because of the sub-recoil velocities associated with Bose condensates. To get an idea of the potential sensitivity of a Sagnac interferometer in this storage ring, we note that the phase sensitivity will be limited by the atomic shot noise, $\sqrt{N}$. Given the $N = 3 \times 10^5$ atoms in the ring and the ~ 100 ms orbiting time, our waveguide could potentially have a measurement sensitivity of $\Delta\Omega = \hbar/4mA\sqrt{N} \sim 10^{-8}$ rad/s from a 1 s long (i.e. 10 lap) measurement. While this figure is nearly 20 times that of existing atom-based gyroscopes [87], improvements such as launching the atoms at higher velocities, increasing the TORT radius, and increasing the atom number may ultimately yield a useful, compact sensing device.

4.10   Bi-directional Propagation in the Circular Waveguide

Any interferometric measurement scheme, with either light or material particles, follows a basic structure: source(s) $\rightarrow$ beamsplitter $\rightarrow$ phase accumulation $\rightarrow$ beamsplitter recombination[3] $\rightarrow$ intensity detection. For viable Sagnac interferometry with atoms in the circular waveguide, all these elements must be demonstrated. With the 3×10^5 atom BEC as the "source," the next step is establishing an atomic beamsplitter in the ring. Ideally, the beamsplitter should take the at rest $|p = 0\rangle$ atomic population and coherently transfer all of the atoms into a superposition of opposing momentum states $(|p = +p'\rangle \pm |p = -p'\rangle)/\sqrt{2}$.[4] The atoms would then propagate about the ring, pass each other on the opposite side, and then recombine at the beamsplitter location. The identical beamsplitting action is reapplied, and the phase-sensitive interference signal is read out.

---

[3]To effect the recombination step a "reflection" is sometimes required. With atoms, this typically is accomplished by a π-pulse (as compared to the $\pi/2$-pulse which serves as the 50/50 beamsplitter).

[4]For atoms confined to the ring, this may be recast in terms of orbital angular momentum states $|L = 0\rangle \rightarrow (|L = +m\rho_o^2\Omega\rangle \pm |L = -m\rho_o^2\Omega\rangle)/\sqrt{2}$.
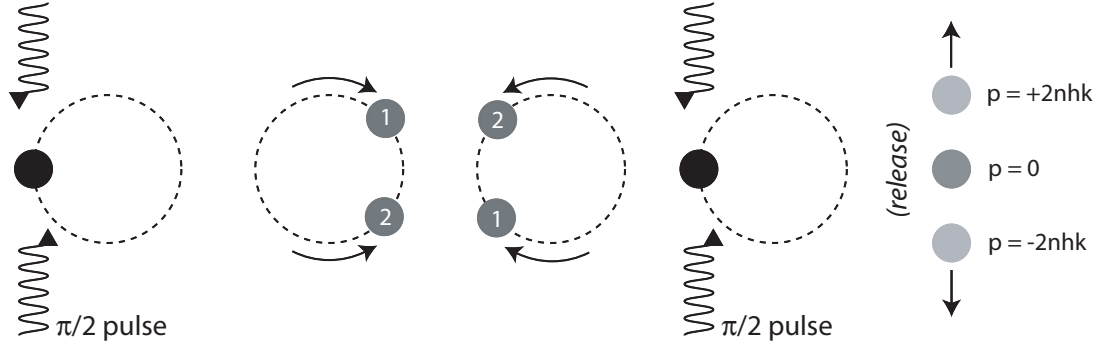
Figure 4.11: Diagram of possible Sagnac interferometry in scheme in a circular waveguide. Counter-propagating optical beams coherently transfer atoms into opposing orbits about the waveguide. The atom pulses (labeled "1" and "2") pass each other on the opposite side and recombine at the origin. The optical beamsplitters are reapplied and the accrued phase difference may be read out, for example, in atomic population differences.

4.10.1   Coherent Atomic Beamsplitters via Light Scattering

Previous attempts to accomplish magnetic beamsplitting, under even more favorable circumstances, proved problematic due to uncontrolled beam filamentation [58, 92]. We look instead to the well-established technique of momentum transfer via light scattering to act as the necessary beamsplitting element, and its proposed use in the circular waveguide is depicted in Figure 4.11. At MIT during the 1980's, fundamental light scattering experiments were conducted which demonstrated Bragg scattering of atoms [93] and Kapitza-Dirac scattering of atoms [94] with off-resonant laser light. The former technique has been used extensively in recent years with Bose condensates [95], both as a spectroscopic tool [96] and as a means of momentum transfer . Bragg scattering could work in this context by overlapping two co-propagating laser beams with a small, coherent frequency difference and then intersecting two such dual-frequency beams at the atoms [97].

A variant of Kapitza-Dirac scattering is a simpler means of doing this. The multiple pulses of light mimic the frequency structure of Bragg scattering beams to give efficient momentum transfer to $|\pm p\rangle$ momentum states, and it has been used in recent interferometry experiments with ultracold atoms in a manner similar to that presented here [98, 99]. In its original presentation, KD scattering was introduced as the deflection of electrons

from a standing wave of light [100]. In the modern context of KD scattering, atoms are diffracted by a standing wave of off-resonant light for a time τ, with the restriction that $\tau \ll 1/\omega_{rec}$ to guarantee that atomic motion is negligible relative to the wavelength of the scattering light. This is the Raman-Nath approximation, and allows the kinetic energy term in the Hamiltonian to be neglected.

To explore this regime to the desired task at hand, we follow the derivation of Ref. [101]. We begin by envisioning an ensemble of atoms illuminated with a laser field of wavevector k, atomic transition detuning $\delta = \omega - \omega_a$, polarization $\hat{\epsilon}$, and magnitude $\mathcal{E}_o$. The field is perfectly retroreflected to yield a standing wave field:

$$
\begin{aligned}
\mathbf{E}(z,t) &= \mathcal{E}_o \sin(kx - \omega t)\hat{\epsilon} + \mathcal{E}_o \sin(kx + \omega t)\hat{\epsilon} \\
&= 2\mathcal{E}_o \sin(kx)\cos(\omega t)\hat{\epsilon}.
\end{aligned}
\tag{4.24}
$$

The field has a single-photon Rabi frequency of $\Omega_R = e\mathcal{E}_o\hat{\epsilon} \cdot \langle e|\mathbf{r}|g\rangle/\hbar$ between the ground state $|g\rangle$ and a single, dominant excited state $|e\rangle$. Finally, the laser field is envisioned to have an envelope of $f(t)$, which sets the time τ that the laser field is "on" by $\tau = \int f^2(t)\,dt$. Assuming the far-detuning limit $|\delta| \gg \Gamma$, where Γ is the linewidth of the $|e\rangle \to |g\rangle$ transition, the interaction Hamiltonian can then be written [101]:

$$
U(z,t) = \frac{\hbar\Omega_R^2}{2\delta}(1 + \cos 2kx)f^2(t).
\tag{4.25}
$$

Under the validity of the Raman-Nath approximation, an initial "at rest" atomic wavefunction $|g, p = 0\rangle$ will evolve to a final atomic wavefunction $|\psi\rangle$ of

$$
\begin{aligned}
|\psi\rangle &= |g,0\rangle \exp\left(-\frac{i}{\hbar}\int U(z,t)\,dt\right) \\
&= |g,0\rangle \exp\left[-i\frac{\Omega_R^2}{2\delta}\tau(1 + \cos 2kz)\right].
\end{aligned}
\tag{4.26}
$$

The presence of the $\cos 2kz$ term in the exponential relates this expression to the well-known Bessel functions of the first order [102], defined by $e^{i\alpha\cos\beta} = \sum\limits_{j=-\infty}^{\infty} i^n J_n(\alpha)e^{in\alpha}$. Thus, Equation (4.26) becomes

$$
|\psi\rangle = e^{-i\frac{\Omega_R^2}{2\delta}\tau} \sum_{j=-\infty}^{\infty} i^n J_n\left(\frac{\Omega_R^2\tau}{2\delta}\right)\left[e^{i2nkz}|g,0\rangle\right].
\tag{4.27}
$$

Noting that $e^{iqx}|p\rangle = |p + \hbar q\rangle$, Equation (4.27) becomes

$$|\psi\rangle = e^{-i\frac{\Omega_R^2}{2\delta}\tau} \sum_{j=-\infty}^{\infty} i^n J_n\left(\frac{\Omega_R^2 \tau}{2\delta}\right) |g, 2n\hbar k\rangle, \qquad (4.28)$$

and the utility of this system becomes evident. After the Kapitza-Dirac scattering "event," the formerly at rest atomic wavefunction $|g, 0\rangle$ is now in a superposition of final momentum states $|g, 2n\hbar k\rangle$ with probability amplitude $J_n^2\left(\frac{\Omega_R^2 \tau}{2\delta}\right)$. This does not immediately have the desired beamsplitting character, but does phase coherently populate opposing momentum states.

More advanced techniques, exploiting the relative phase accumulation $e^{i2n^2\hbar k^2 t/m}$ of each populated momentum state under free evolution, can even effect near unity transfer of atomic ensembles to specific opposing momentum states, i.e. $|g, 0\rangle \rightarrow (|g, 2n\hbar k\rangle + i|g, -2n\hbar k\rangle)/\sqrt{2}$, exactly the desired beamsplitter functionality [98, 103]. With a reliable KD beamsplitter, the Sagnac experiment in the ring could be carried out just as depicted in Figure 4.11.
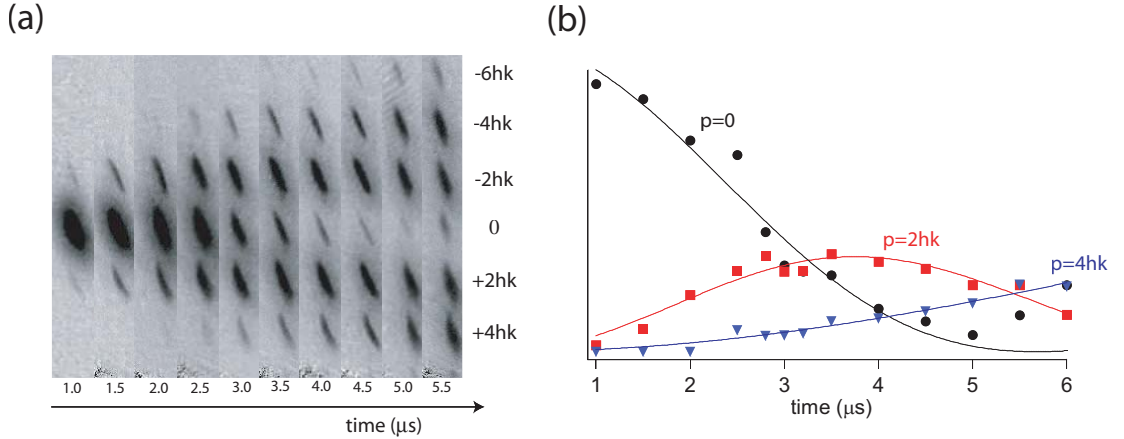

Figure 4.12: Kapitza-Dirac Scattering in the Ring. The KD pulse (a) As described in text, probabilities of populating the nth momentum order is $J_n^2\left(\frac{\Omega_R^2 \tau}{2\delta}\right)$. 30 ms TOF imaging shows the scattering into higher momentum orders as the KD pulse time is increased. (The skewed appearance of the clouds is due to imperfect alignment of the KD beam with the trapping axes.) (b) Number counting of spatially separated momentum populations agrees well with the expected Bessel functions (solid curves).

4.10.2   Kapitza-Dirac Scattering in the Ring

We begin by demonstrating "normal" KD scattering, accomplished by illuminating the trapped atoms and then observing the populations of the separated wavepackets. Figure 4.12 shows the expected Bessel function population of momentum orders under time-of-flight imaging.

With the demonstrated ability to populate high-order momentum states, we attempted to send wavepackets in opposing directions about the ring. The balancing act is a fine one indeed, as the recoil energy for the first and second orders are $E_{2\hbar k} = 710\,\text{nK}$ and $2.85\,\mu\text{K}$, respectively, both less than the $5\,\mu\text{K}$ azimuthal energy profile measured in Figure 4.9. For this reason, the BEC needs to originate at the top of this potential curve before the KD pulse outcouples the momentum states to crest over the potential maxima.

Figure 4.13 shows a time-sequence of bidirectional propagation, as multiple momentum orders are set into motion. The technique successfully established bidirectional propagating in all but the $\pm 2\hbar k$ pulses, with the $4\hbar k$ exhibiting the highest contrast (and only visible full orbit recombination). Ultimately, the observation was compromised by the numerous momentum states occupying the ring, the spread of the wavepackets over the relatively long orbiting times, and perhaps collisions. The latter factor is difficult to quantify as it is not known if the pulses are in the same transverse state (i.e. ground state vs. oscillating coherent state). If 10^5 atoms at $\pm 2\hbar k$ pulses *were* to collide while in the transverse ground state after a half orbit, the collisional rate would be of the order $200\,\text{Hz}$. This would predict approximately 4 collisions per atom on a single pass, which would bring both beams to an effective halt in the $5\mu\text{K}$ ring. As considered, he collisional probability per pass is independent of velocity, and the fact that the $4\hbar k$ pulses pass each either renders this analysis moot or speaks a transverse excitation which vastly reduces this collision rate.

It should be clear from Figures 4.12 and 4.14 that "normal" KD scattering does not at all act as the desired beamsplitting element because of the inability to split the population into specific $\pm 2n\hbar k$ momentum orders with high efficiency. Wu *et al.* [103] report a modified KD scattering technique which can, in principle, transfer nearly the entire $p = 0$ population to a specific $p = \pm 2n\hbar k$ order with very high efficiency[5]. We attempted to

---

[5]Ref. [103] reports maximum theoretical fidelities of 99.99% for $n = 1$, 99.1% for $n = 2$, 96.6% for $n = 3$,
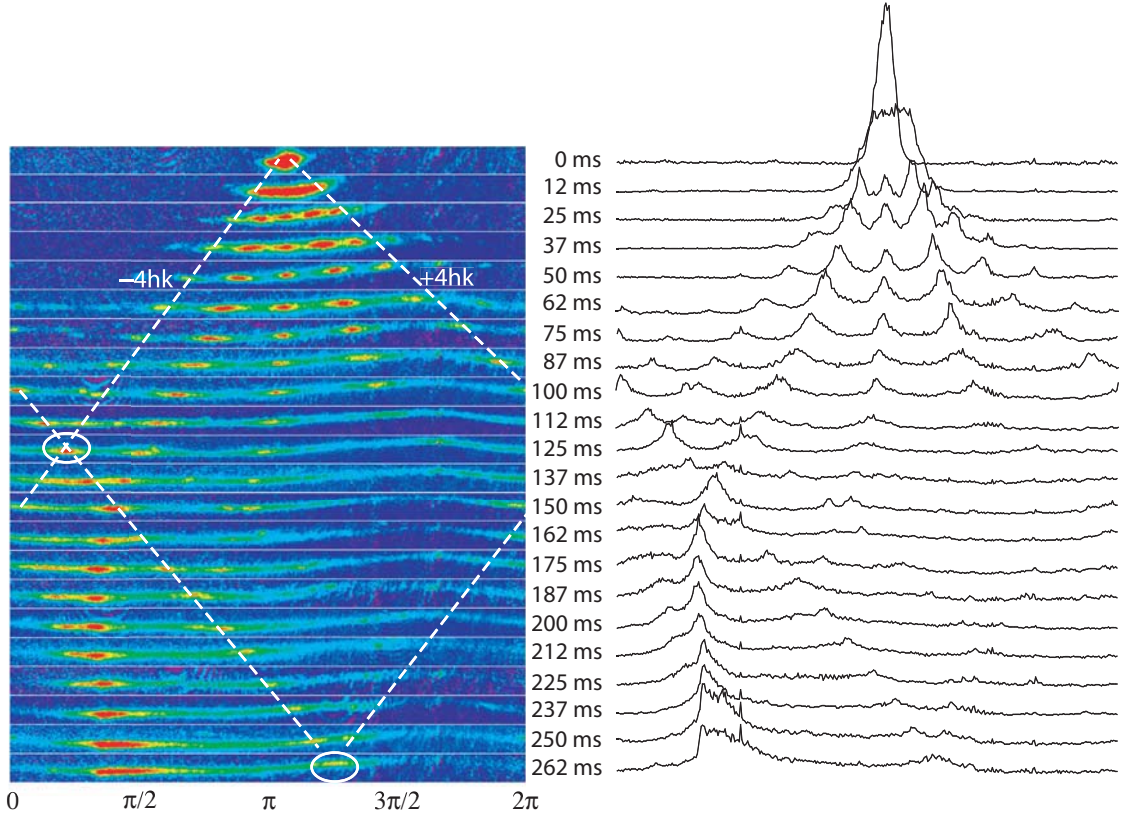
Figure 4.13: Bidirectional propagation in the ring via Kapitza-Dirac scattering. After a KD pulse which populates numerous momentum orders, we may observe their motion about the ring. All momentum orders $n \geq 2$ had enough kinetic energy to overcome the potential variations $U(\theta)$. The dotted lines guide the eye with the $\pm 4\hbar k$ pulses which can be seen crossing on the "far side" at $t = 125\,\mathrm{ms}$ and finally recombining near the origin. That the pulses did not meet up *at* the origin implies some small net velocity at the start of the launch. Note the apparent potential valley from $\frac{3\pi}{2} \lesssim \theta \lesssim \pi$ and the potential maximum at $\theta \approx \frac{\pi}{2}$, exactly the azimuthal potential structure seen in Figure 4.9.

implement this technique, which is basically a two-pulse KD sequence with four parameters, the Rabi frequency Ω_R, the first pulse time τ_1, a wait time τ_w, and a second pulse time τ_2. The principle which allows this is a multipath interference effect between the amplitudes $C_n = \frac{1}{\sqrt{2}} \left(c_n + c_{-n}\right)$, where c_n is the amplitude of the momentum state $|p = 2n\hbar k\rangle$. Ideally, the pulse sequence inverts the population between the zero-momentum state and some non-zero momentum order n', i.e. $C_0 = 1, C_{n \neq 0} = 0 \rightarrow C_{n'} = 1, C_{n \neq n'} = 0$. The Raman-Nath

and 91.7% for $n = 4$

regime equations discussed earlier, coupled with the free evolution phases $e^{-i2n^2\hbar k^2 t/m}$ allow a large enough parameter space such that proper values of Ω_R, τ_1, τ_w, and τ_2 yield mostly constructive interference for the $C_{n'}$ and destructive interference for $C_{n\neq n'}$.

In practice, while this prescription did not yield the optimal efficiencies, it was efficacious in vastly improving the momentum transfer to specific diffraction orders. Figure 4.14 shows images of this procedure enacted for the first- and second-orders.
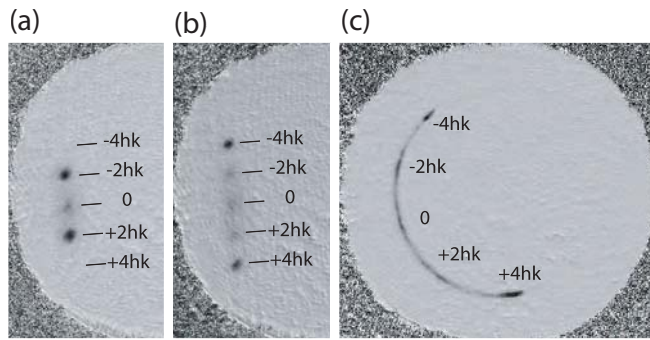

Figure 4.14: Resonant Kapitza-Dirac scattering into specific momentum modes. Using two pulse techniques [103], majority populations are driven into (a) $\pm 2\hbar k$ and (b) $\pm 4\hbar k$, as seen in 25 ms time-of-flight. (c) The same pulse in (b) is applied and atoms are allowed to propagate in the ring with enough energy to overcome the azimuthal potential variations. The sizeable remainder of 0 and $\pm 2\hbar k$ populations, as well as the unbalanced $\pm 4\hbar k$ populations, is typical for these experiments and shows the limitations of the resonant transfer in this implementation.

Unfortunately, the multiple pulse method did not prove to be robust in our experiments, as wide variances in transfer efficiency were observed shot-to-shot. Other techniques were attempted such as modulating the intensity KD pulse at the $n = 2$ Bragg resonance, but we observed similarly sporadic and inefficient experimental results. The fact that the initial beamsplitter was unreliable gave little hope that we would be able to demonstrate the second recombining pulse necessary for a Sagnac interferometer in this first iteration of the ultracold atom storage ring. We look forward to advances on this front in other more experiments in circular waveguides, perhaps even the second generation of this particular implementation.